This is a preprint, the final version is subject to change, of the American Mineralogist (MSA)
Cite as Authors (Year) Title. American Mineralogist, in press.
(DOI will not work until issue is live.) DOI: http://dx.doi.org/10.2138/am.2014.4748

Revision 1

Role of silica for the progress of serpentinization reactions: Constraints from successive changes in mineralogical textures of serpentinites from Iwanaidake ultramafic body, Japan

Akane Miyoshi[1,*], Tetsu Kogiso[1,†], Naoto Ishikawa[1], and Kenji Mibe[2]
[1]Department of Interdisciplinary Environment, Graduate School of Human and Environmental Studies, Kyoto University, Kyoto 606-8501, Japan
[2]Earthquake Research Institute, University of Tokyo, Tokyo 113-0032, Japan
* Present address: JX Nippon Oil and Energy Corporation, Kawasaki 210-0863, Japan
† Corresponding author: kogiso@gaia.h.kyoto-u.ac.jp

Abstract

Serpentinization of peridotite in subduction zones and mid-ocean ridges is a key process that significantly controls not only the geodynamic behavior of the mantle but also the activity of modern (and probably primordial) microbial systems on the seafloor. However, there is still controversy about what factors promote the mineralogical reactions of serpentinization in natural ultramafic rocks. Here we report textures, chemistry, and magnetic susceptibility of variably serpentinized harzburgite and dunite samples from Iwanaidake ultramafic body, Japan, which originated from the forearc mantle of the Northeast Japan arc. Successive changes in textures, mineral chemistry, and magnetic susceptibility during serpentinization of harzburgite involved two stages: replacement of olivine by serpentine and brucite, and subsequent formation of magnetite along with more-magnesian serpentine and brucite. The later reactions occurred concurrently with serpentinization of orthopyroxene, which supplied the silica component. In serpentinized dunite, which doesn't contain orthopyroxene, serpentinization involved replacement of olivine by serpentine and brucite, and the fraction of magnetite did not increase with the progress of serpentinization. These observations suggest that the silica supply from serpentinization of orthopyroxene is an essential factor for the formation of magnetite during serpentinization. Magnetite formation facilitated by addition of silica has often been reported for

many serpentinite systems, suggesting that the magnetite formation triggered by silica addition is one of the key reactions for the progress of serpentinization in natural ultramafic rocks.

Keywords: serpentine, magnetite, magnetic susceptibility, bulk H_2O content, mineralogical texture

Introduction

The transformation of mantle peridotite into serpentinite changes the physical properties of the mantle, such as seismic velocity, density, magnetic susceptibility, electric conductivity, and viscosity (e.g., Toft et al. 1990; Dyment et al. 1997; Escartin et al. 1997; Mèvel 2003; Katayama et al. 2009; Hirauchi et al. 2010). Serpentinization also produces hydrogen, which is essential for the establishment of microbial communities in serpentine-hosted hydrothermal fields on the seafloor (e.g., Takai et al. 2004; Nealson et al. 2005). It is now generally thought that microbial activities associated with serpentine-hosted hydrothermal systems played a key role in the genesis of life in the early oceans (e.g., Sleep et al. 2004; Martin et al. 2008).

Recent petrologic studies have proposed that serpentinization reactions proceed via a two-stage process involving the early formation of serpentine + brucite and subsequent magnetite formation (e.g., Toft et al. 1990; Bach et al. 2006; Beard et al. 2009). Magnetite, which is the key mineral controlling the magnetic properties, electrical conductivity, and density of peridotite, as well as the efficiency of hydrogen production, is thought to be formed by the second-stage reaction, but there remains considerable controversy regarding what factors promote the formation of magnetite (e.g., Oufi et al. 2002; Bach et al. 2006; Frost and Beard 2007; Beard et al. 2009; Plümper et al. 2012; Frost et al. 2013). Bach et al. (2006) and Beard et al. (2009) proposed that magnetite is formed by the breakdown of brucite promoted by the addition of aqueous silica:

brucite + silica = serpentine + magnetite + water + hydrogen.

Conversely, Katayama et al. (2010) suggested that magnetite is formed by the breakdown of ferroan serpentine, which results in the production of silica component:

serpentine = magnetite + silica + water + hydrogen.

In contrast, Evans (2008, 2010) suggested that the Fe-Mg exchange potential of olivine and the variability of Fe^{3+} in serpentine minerals are key factors to control the formation of magnetite.

One of the clues to solve this controversy is the successive change in mineralogical textures with the progress of serpentine reactions, which will allow us to constrain the reactions responsible for the progression of serpentinization, because multistage serpentinization processes are expected to produce different textures in serpentinites at each stage of the reaction. Textural changes with the progress of serpentinization have been described in previous studies (e.g., Bach et al. 2006; Beard et al. 2009; Frost et al. 2013), but those studies have only focused on highly serpentinized samples, or have examined just a small number (<4) of serpentinized samples. In this study, we examine 40 samples of variably (0% to 100%) serpentinized peridotite taken from the Iwanaidake ultramafic body in Kamuikotan belt, Hokkaido, Japan. We describe successive changes in textures, mineral chemistry, magnetic properties and H_2O contents of these samples, and discuss the processes responsible for the progression of serpentinization and magnetite formation.

Geological setting

The Kamuikotan belt, located in the central axial part of Hokkaido, Japan, is a part of orogenic zone formed by the collision of Northeast Japan arc and Kuril arc during the Mesozoic (Kimura 1986). It consists of high- and low-pressure metamorphic rocks and subordinate volumes of ultramafic rocks (Ishizuka et al. 1983). The Iwanaidake ultramafic body is found in the southern

78 part of the Kamuikotan belt. Katoh (1978) called the ultramafic rocks in this area the "Saru-gawa
79 ultramafic massif" and divided it into eastern and western units. The western unit will be referred
80 as the "Iwanaidake ultramafic body" in this study.

81 A fresh peridotite domain, measuring about 1 km diameter, occurs at the top of Mt.
82 Iwanaidake, within the Iwanaidake ultramafic body. It is composed of harzburgite accompanied
83 by a small volume of dunite. Dunite occurs in harzburgite as dyke-shaped or lens-shaped bodies.
84 Generally, boundaries between dunite and harzburgite are sharply defined. The ultramafic rocks
85 surrounding the peridotite domain, measuring about 3 km wide and > 10 km long, are partly or
86 completely serpentinized, with the degree of serpentinization increasing gradually as one moves
87 farther away from the peridotite domain. The central peridotite and surrounding serpentinite are
88 thought to originally have had the same lithology based on the similarities found in chemical
89 compositions of relic minerals and inclination of the serpentine layers (Katoh, 1978). Katoh and
90 Nakagawa (1986) noted that this complex was a section characterized by remarkably depleted
91 ophiolites. However, a petrochemical study by Kubo (2002) argued that the highly depleted
92 dunite may have formed by intensive incongruent melting of harzburgite triggered by the
93 injection of hydrous melts in the host harzburgite. This model suggests that the Iwanaidake
94 peridotite may have been emplaced in the mantle wedge of a subduction zone where hydrous
95 melts can form and upwell (Kubo, 2002).
96
97 **Petrography**

98 From the Iwanaidake ultramafic body, we collected 25 harzburgite and 15 dunite samples,
99 which include non-serpentinized peridotite and partly to totally serpentinized rocks. Mineral
100 assemblage and textures were investigated with optical microscopy and a laser Raman
101 spectroscope JASCO NRS-3100 at the Department of Geology and Mineralogy, Kyoto

University. Raman analysis was performed using a green laser (532 nm wave length) and 1.2 s integration time. The modal compositions were determined by counting 2000 points. The degree of serpentinization was defined as the total mode of serpentinized portions (i.e., total volume fractions of serpentine, brucite and magnetite). The modal compositions of the samples are listed in Table 1. Major element compositions of minerals were analyzed using an electron microprobe JEOL JXA-8105 at the Department of Geology and Mineralogy, Kyoto University, with a 3 μm beam of 15 kV acceleration voltage, 10 nA beam current, and 10 s peak acquisition time for all elements. Standard materials used are wollastonite for Si and Ca, rutile for Ti, corundum for Al, synthetic Cr_2O_3 for Cr, hematite for Fe, rhodonite for Mn, synthetic MgO for Mg, pentlandite for Ni, albite for Na, and potassium feldspar for K. Standard deviations (1 sigma) are less than 0.8 wt% for all elements. The analyzed mineral compositions are listed in the Supplementary table.

Serpentinized harzburgite

Harzburgite consists of olivine, orthopyroxene, and accessory Cr-spinel and clinopyroxene. Average Mg# (molar Mg/(Mg + Fe) x 100) of olivine and orthopyroxene is 92. Serpentinized harzburgite consists mainly of serpentine, brucite, magnetite, and relic minerals (Table 1). Partially or completely serpentinized olivine crystals exhibit typical mesh texture: a serpentine mesh rim with relic or serpentinized olivine mesh center. Some samples have serpentine ± magnetite veins that cut through all textures, which is indicative of their having been formed at a very late stage in serpentinization. Raman spectra of serpentine minerals in the mesh textures have weak bands around 510–520 cm^{-1}, suggesting that they are lizardite and/or antigorite (Rinaudo et al. 2003). However, it is difficult to strictly confirm the serpentine phases because the positions of bands around 680–690 and 1,000–1,100 cm^{-1}, which are key bands to distinguish antigorite from lizardite (Rinaudo et al. 2003), are poorly constrained.

A notable feature of the serpentinized harzbugite samples is that there are two types of mesh rims (Figure 1): the brown colored area (type-A rim) is an intimate mixture of serpentine and brucite, whereas the colorless area (type-B rim) is composed solely of serpentine. In samples that have both type-A and B rims, the type-A rims always occupy the innermost area in contact with relic olivine, and type-B rims occupy the surrounding area (Figure 1a, b). Serpentine in type-A rims displays negative elongation (α-serpentine), while that in type-B rims displays positive elongation (γ-serpentine). Type-B rims are always accompanied by brucite-magnetite veins in the outermost part of the mesh texture (i.e., the brucite-magnetite veins are found sandwiched between adjacent type-B rims: Figure 1b-c).

Chemical compositions of type-A rims form a trend connecting relic olivine (Mg#92), serpentine (Mg#94) and brucite (Mg#86) on the FeO–MgO–SiO_2 ternary diagram (Figure 2) and the (Si + Al/2 + Cr/2)–total Fe cation plot (Figure 3a). This trend indicate that the serpentine in type-A rims doesn't contain Mg-cronstedtite ($Mg_2Fe^{3+}{}_2SiO_5(OH)_4$) or cronstedtite ($Fe^{2+}{}_2Fe^{3+}{}_2SiO_5(OH)_4$) component. Type-B rims are composed solely of serpentine with variable Mg# (Mg#93–96). The Fe-rich end of type-B rim serpentine plots along a trend toward Fe^{3+}-serpentine ($Fe^{3+}{}_2Si_2O_5(OH)_4$) (Figures 2 and 3b), suggesting that Fe in the type-B rim serpentine is partly ferric. Compositions of brucite in brucite-magnetite veins were not precisely determined owing to the narrow width of the veins, but the analyzed data plot along a trend connecting the Mg-rich end of type-B rim serpentine (Mg#96) and brucite (Mg#89) (Figure 2), suggesting that the brucite-magnetite veins contain Mg#89 brucite, which is more magnesian than that in type-A rims.

Serpentinized portion of mesh centers contains small grains of magnetite (Figure 1d). Compositions of mesh-center serpentine are variable Mg# (90–93), which is less magnesian than that of type-B rims (Figures 2, 3b-c). Serpentinized orthopyroxene (called “bastite”) are found in

highly serpentinized samples. Most of bastite is composed solely of serpentine, but bastite in some samples sporadically contains aggregates of magnetite grains, which may have formed along with oxidation of Cr-spinel inclusions in orthopyroxene. Mg# of bastite ranges from 82 to 92 (Figures 2, 3d). The variations of mesh-center serpentine and bastite also form trends toward Fe^{3+}-serpentine (Figures 2, 3c–d), suggesting some contribution of ferric iron in mesh-center serpentine and bastite as well as in type-B rims.

The modal compositions of textures change systematically as serpentinization progresses (Figure 4a). The change in modal compositions shows that the mode of type-A rims is higher in weakly serpentinized samples (0 to ~40 vol%), whereas the mode of type-B rims increases while that of type-A rims decreases with increasing degree of serpentinization (Figure 4a). It should be noted that type-B rims appear concurrently with serpentinization of orthopyroxene and mesh center at a similar degree of serpentinization.

Serpentinized dunite

Dunite consists of olivine and Cr-spinel. Serpentinized dunite consists of serpentine, brucite, magnetite and relic minerals (Table 1). Unlike serpentinized harzburgite, mesh rims of dunite consist mostly of type-A rims. Very small amounts of magnetite are sparsely distributed in mesh rims and mesh centers. The chemical compositions of type-A rims are the same as those in harzburgite (Figure 3a). The chemical compositions of mesh-center serpentines are similar to those of type-A rims (Figures 3a, c). There is no indication of the presence of ferric iron in both mesh rims and centers. The late-stage serpentine veins are also observed, and magnetitized spinel crystals are observed in highly serpentinized samples.

The mode of type-A rims in dunite increases as serpentinization progresses, and type-B rims are rarely present, except for small amounts seen in moderately serpentinized samples (Figure

4b). The mode of mesh-center serpentine gradually increases together with that of type-A rims. This is in contrast to the case in serpentinized harzburgite where the mode of mesh-center serpentines remains low even in highly serpentinized samples.

Bulk magnetic susceptibility and H_2O content

Bulk magnetic susceptibility, which is an indicator of the fraction of magnetite (e.g., Toft et al. 1990), was measured by a KLY-3S Spinner Kappabridge at Department of Interdisciplinary Environment, Kyoto University. Samples were cut into 2 x 2 x 2 cm cubes and the magnetic susceptibility for each sample was measured at 300 A/m rms field intensity and 875 Hz operating frequency of the magnetic field. The measured susceptibility values are listed in Table 1. The bulk magnetic susceptibility values of highly serpentinized harzburgite (serpentinization exceeding 30 vol%), which have type-B rims and bastite, are higher than those of weakly serpentinized harzburgite (Figure 5). In contrast, the magnetic susceptibility of serpentinized dunite remains constant even as serpentinization progresses.

Bulk H_2O content was measured by an ADP-512 Karl Fisher moisture titrator at the Earthquake Research Institute, University of Tokyo. After being heated at 120°C to remove any moisture absorbed from air, each powdered sample (~100 mg) was heated at 1000°C for 15–20 minutes until no further release of moisture could be observed. The bulk H_2O contents in serpentinized dunite and harzburgite samples (Table 1, Figure 6) exhibit similar trends until moderate degree of serpentinization, while the H_2O contents of serpentinized harzburgite are lower than those of dunite at higher degrees of serpentinization.

Discussion

Serpentinization reactions in harzburgite

198 The modal changes in mineralogical texture types in serpentinized harzburgite (Table 1,
199 Figure 4a) demonstrate that type-A rims occur more abundantly in weakly serpentinized samples,
200 and that increase in the modes of type-B rims and bastite is concurrently initiated at a moderate
201 degree (~30 vol%) of serpentinization. This indicates that the process of serpentinization takes
202 place in two stages: first, the formation of the type-A rim replacing olivine, and then, the later
203 formation of the type-B rim and bastite. The higher values of magnetic susceptibility in highly
204 serpentinized samples (Figure 5) suggest that the magnetite formation occurs in the later stage of
205 serpentinization. Such two-stage serpentinization processes have been documented in many
206 serpentinite systems (Bach et al. 2006; Beard et al. 2009; Frost et al. 2013). Here we propose
207 mineral reactions responsible for the two-stage serpentinization process in the Iwanaidake body
208 on the basis of the modal changes and compositional relationships of the minerals.

209 **First-stage serpentinization.** Chemical compositions of type-A rims form a trend that
210 connects relic olivine, Mg#94 serpentine, and Mg#86 brucite (Figure 2, 3a). This trend and the
211 paucity of magnetite in poorly serpentinized samples indicate an isochemical reaction without
212 forming magnetite during the first-stage serpentinization:

213

214 $$2Mg_{1.84}Fe_{0.16}SiO_4 + 3H_2O = Mg_{2.82}Fe_{0.18}Si_2O_5(OH)_4 + Mg_{0.86}Fe_{0.14}(OH)_2 \quad (1)$$

215 Mg#92 olivine + water = Mg#94 serpentine + Mg#86 brucite.

216

217 Most of the analyzed data of type-A rims plot only between relic olivine and serpentine (Figure
218 3), implying that the bulk composition of type-A rims would be richer in silica than original
219 olivine, that is, silica would have been added to olivine during the formation of type-A rims.
220 However, the compositional trend of type-A rims doesn't deviate toward SiO_2 (Figure 3a),
221 indicating that no silica addition occurred during type-A rim formation. The apparent silica

enrichment is probably due to sampling bias in electron microprobe analysis. When analyzing type-A rims by the electron microprobe, we spotted relatively flat portions of the rims. Since brucite is weaker against polishing than serpentine, brucite-rich portions in the type-A rims tend to have rough surface compared with serpentine-rich portions. As a consequence, we selectively analyzed serpentine-rich portions of the type-A rims, resulting in the apparent silica enrichment.

Second-stage serpentinization.

The second stage of the serpentinization process is accompanied by increase in the modes of type-B rims and brucite-magnetite veins and decrease in type-A rims (Figures 1, 4a). This indicates that during the second stage the type-A rims are replaced by the type-B rims and brucite-magnetite veins. Brucite in the brucite-magnetite veins is more magnesian than that in type-A rims (Figure 2). Although serpentine of type-B rims heterogeneously contains a certain amount of $Fe^{3+}_2Si_2O_5(OH)_4$ component (Figure 3b), the analyzed data of coexisting brucite-magnetite veins form a trend connecting Mg#96 serpentine (= Mg-rich end of type-B rim serpentine) and Mg#89 brucite (Figures 2 and 3b), suggesting that Mg#96 serpentine mainly formed in type-B rims. The concurrent appearance of type-B rims and brucite-magnetite veins accompanied by bastite formation (Figure 4a) suggests that the formation of type-B rims and brucite-magnetite veins proceeded by the supply of silica from bastite formation as follows:

$$Mg_{2.82}Fe_{0.18}Si_2O_5(OH)_4 + Mg_{0.86}Fe_{0.14}(OH)_2 + X\,SiO_2(aq) = (1 + 0.5X)Mg_{2.88}Fe_{0.12}Si_2O_5(OH)_4 + (0.90 - 1.62X)Mg_{0.89}Fe_{0.11}(OH)_2 + (0.03 + 0.04X)Fe_3O_4 + (0.07 + 0.58X)H_2O + (0.03 + 0.04X)H_2 \quad (2)$$

Mg#94 serpentine + Mg#86 brucite + silica = Mg#96 serpentine + Mg#89 brucite + magnetite + water + hydrogen.

246 $3Mg_{0.92}Fe_{0.08}SiO_3 + 2H_2O = Mg_{2.76}Fe_{0.24}Si_2O_5(OH)_4 + SiO_2(aq)$ (3)

247 Mg#92 orthopyroxene + water = Mg#92 serpentine + silica.

248

249 Mesh-center serpentinization also occurred concurrently with bastite formation (Figure 3a),
250 suggesting that the silica from reaction 3 also facilitated serpentinization of mesh center:

251

252 $Mg_{1.84}Fe_{0.16}SiO_4 + 1.33H_2O + 0.32SiO_2(aq) = 0.66Mg_{2.79}Fe_{0.21}Si_2O_5(OH)_4 + 0.01Fe_3O_4 +$

253 $0.01H_2$ (4)

254 Mg#92 olivine + water + silica = Mg#93 serpentine + magnetite + hydrogen.

255

256 **Formation of ferric serpentine.** As well as type-B rim serpentine, bastite and mesh-center
257 serpentine also contain significant amounts of $Fe^{3+}{}_2Si_2O_5(OH)_4$ component (Figures 2, 3b-d).
258 Therefore, the supply of silica by bastite formation (reaction 3) should have partly contributed to
259 generate $Fe^{3+}{}_2Si_2O_5(OH)_4$ component in addition to magnetite. If we assume that all the iron in
260 the product of reaction 2 was incorporated in serpentine as ferric iron, then the reaction can be
261 deduced from mass balance as follows:

262

263 $Mg_{2.82}Fe^{2+}{}_{0.18}Si_2O_5(OH)_4 + Mg_{0.86}Fe_{0.14}(OH)_2 + 0.77SiO_2(aq) =$

264 $1.39Mg_{2.65}Fe^{3+}{}_{0.23}Si_2O_5(OH)_4 + + 0.07H_2O + 0.16H_2$ (5)

265 Mg#94 serpentine + Mg#86 brucite + silica = Mg#92 $MgFe^{3+}$-serpentine + water + hydrogen.

266

267 Mg# of the Fe^{3+}-bearing serpentine produced by this reaction is 92, which is close to that of the
268 most Fe-rich serpentine in type-B rims (Figure 3b), suggesting that the most Fe-rich serpentine in

type-B rims can form by this reaction without forming magnetite.

To produce Fe-rich bastite containing Fe^{3+}-serpentine component, supply of iron is necessary, because simple addition of water to the relic orthopyroxene (Mg#92) cannot produce Fe-rich bastite with Mg# <92. If the ferric iron is supplied as magnetite, the reaction to form the most Fe-rich (Mg#82) bastite is:

$$3Mg_{0.92}Fe_{0.08}SiO_3 + 0.12Fe_3O_4 + 2.44H_2O = 1.22Mg_{2.26}Fe^{3+}_{0.49}Si_2O_5(OH)_4 + 0.56SiO_2(aq) \quad (6)$$

Mg#92 orthopyroxene + magnetite + water = Mg#82 $MgFe^{3+}$-serpentine + silica.

Similarly, the most Fe-rich composition of mesh-center serpentine (Mg#90) can form by the following reaction, if the ferric iron is supplied as magnetite:

$$Mg_{1.84}Fe_{0.16}SiO_4 + 0.02Fe_3O_4 + 1.52H_2O + 0.43SiO_2(aq) = 0.72Mg_{2.57}Fe^{3+}_{0.29}Si_2O_5(OH)_4 + 0.09H_2 \quad (7)$$

Mg#92 olivine + magnetite + water + silica = Mg#90 $MgFe^{3+}$-serpentine + hydrogen.

Magnetite for these two reactions can be supplied from reaction 2, which requires supply of silica from bastite formation (reaction 3). Thus, silica released from bastite formation was consumed by the formation of type-B rims and brucite-magnetite veins (reaction 2), and the magnetite produced there was in turn partly consumed in bastite and mesh-center serpentine formation (reactions 6, 7).

Evans (2008) demonstrated that highly serpentinized peridotites tend to have higher ferric iron/total iron ratios, and suggested that more than half of the ferric iron in the system is

292 contained in serpentine. In Iwanaidake body, however, the higher magnetic susceptibility in the
293 second stage harzburgites (Figure 5) shows that significant amounts of magnetite formed during
294 the second stage, suggesting that ferric iron produced in the second stage was mainly
295 incorporated in magnetite. Since Fe^{3+}-serpentine-forming reactions 5–7 don't form magnetite but
296 consume magnetite, it is likely that Fe^{3+}-serpentine-free reactions (reactions 2–4) dominantly
297 proceeded in the second stage serpentinization of harzburgite in the Iwanaidake body.
298

299 **Serpentinization reactions in dunite**

300 The modal changes in mineralogical texture types in serpentinized dunite (Figure 4b)
301 demonstrate that type-A rims and mesh-center serpentine were dominantly produced with the
302 progress of serpentinization. No significant increase in magnetite mode can be observed (Table
303 1), as evidenced by the relatively constant magnetic susceptibility (Figure 5). The chemical
304 compositions of mesh-center serpentine of dunite are similar to type-A rims (Figures 2, 3),
305 suggesting that serpentinization in dunite occurs only through reaction 1.
306

307 **The progress of two-stage serpentinization**

308 Progress of serpentinization reactions and associated changes in mineralogical textures in the
309 Iwanaidake ultramafic body are schematically illustrated in Figure 7. In harzburgite, type-A rims
310 (serpentine + brucite) were formed by isochemical serpentinization of olivine (reaction 1) during
311 the first stage. This reaction was promoted by the addition of aqueous fluids. Type-B rims
312 (serpentine), brucite-magnetite veins, and mesh-center serpentine and magnetite were formed
313 during the second stage (reactions 2 and 4). Magnetite and hydrogen were produced during this
314 stage. These reactions were facilitated by the addition of aqueous silica released by
315 serpentinization of orthopyroxene (reaction 3), which partly contributed to form Fe^{3+}-serpentine

316 component (reactions 5–7). In dunite, a single-stage serpentinization occurred: type-A rims and
317 mesh-center serpentine and brucite were formed by isochemical serpentinization of olivine
318 (reaction 1). Magnetite and hydrogen were not produced in dunite due to the absence of
319 orthopyroxene, which can supply silica during serpentinization.

320 In weakly serpentinized harzburgites, the second-stage reactions didn't occur, although they
321 contain significant amounts of orthopyroxene (up to 20 vol%, Figure 4a), suggesting that the
322 second-stage serpentinization is triggered by serpentinization of orthopyroxene. The later
323 hydration of orthopyroxene is a key for understanding why serpentinization reactions proceeded
324 via two stages. One possible explanation for the later hydration of orthopyroxene is the change of
325 temperature during serpentinization. Thermodynamic calculations (e.g., Frost and Beard, 2007;
326 Klein et al. 2009) and experimental studies (e.g., Martin and Fyfe, 1970; Allen and Seyfried,
327 2003) have demonstrated that hydration of orthopyroxene occurs at temperatures higher than
328 hydration of olivine. Therefore, the second-stage serpentinization in the Iwanaidake body may
329 have occurred at temperature higher than the first-stage, that is, the two-stage serpentinization
330 process may have proceeded with increasing temperature, although further evidence for the
331 change of temperature condition during serpentinization of Iwanaidake body is needed.

332

333 **Variations in bulk magnetic susceptibility and H_2O content**

334 We tested whether the serpentinization reactions proposed here (reactions 1–4, Figure 7) can
335 explain the variations in the bulk magnetic susceptibility and H_2O content (Figures 5, 6). We have
336 used the method introduced by Toft et al. (1990) to calculate how magnetic susceptibility would
337 change with increasing fraction of magnetite. According to this method, the magnetic
338 susceptibility of bulk rock is given by the equation, $K = 3.2\ F$, where K is the SI (the International
339 System of Units) values of magnetic susceptibility of bulk rock, and F is the volume content of

magnetite.

Changes in magnetic susceptibility and bulk H_2O content with the progress of the reaction 1 (first stage) and reactions 2–4 (second stage) were calculated assuming the following: that the modal composition of protolith dunite is 100 vol% olivine, and that of harzburgite is 83 vol% olivine and 17 vol% orthopyroxene; that the second reaction starts when the degree of serpentinization reaches 30 vol%; and that the fraction of SiO_2 supplied in the second stage (X of reaction 2) was 0.4. The calculated magnetic susceptibility and bulk H_2O content are shown as arrows in Figures 5 and 6, respectively. The calculated magnetic susceptibility of the second stage increases because of the formation of magnetite by reactions 2 and 4. This is consistent with the measured magnetic susceptibility being higher in the second-stage harzburgites than in the first-stage ones (Figure 5). In contrast, the calculated magnetic susceptibility of the first stage does not increase with the progress of serpentinization because no magnetite forms. This is also consistent with the measured magnetic susceptibility of dunite, which is kept relatively constant (Figure 5). The calculated trends of magnetic susceptibility are not wholly consistent with those of the measured values, but this may be attributed to the fact that the magnetic susceptibility is a rough approximation of the fraction of magnetite and is not strictly proportional to the mode of magnetite. Indeed, magnetic susceptibility is influenced by other parameters such as grain size distribution of magnetite (e.g., Maher 1998; Dearing 1999). Oxidation and/or alteration of magnetite also affect the relationship between magnetic susceptibility and magnetite mode. Low magnetic susceptibility in very highly (more than 90%) serpentinized harzburgites (Figure 5) could be due to oxidation or alteration of the magnetite that had been formed at the second-stage serpentinization reactions, although the degrees of oxidation/alteration of magnetite have not been assessed.

The trends of the calculated H_2O content roughly match those of the measured H_2O contents

for both harzburgite and dunite (Figure 6). The calculated H_2O content for the second-stage serpentinization is lower than that of the first-stage (broken arrow of Figure 6), because the replacement of Fe-rich brucite by reaction 2 suppresses the increase of bulk H_2O content. This is consistent with the observation that the rate of increase in H_2O content in harzburgite is lower in highly serpentinized samples whereas the H_2O content in dunite increases linearly (Figure 6). The measured H_2O contents of moderately serpentinized samples are systematically higher than the calculated trends. This discrepancy is probably due to heterogeneous distribution of late-stage serpentine veins in these samples, which were not completely removed during preparation of powders for H_2O analysis.

Thus, the changes in bulk magnetic susceptibility and H_2O content during serpentinization can be sufficiently explained by our model that serpentinization takes place in two stages in harzburgite and a single stage in dunite.

Role of silica for magnetite formation

Our observations suggest that magnetite formation during the second-stage serpentinization of harzburgite requires a supply of aqueous silica, as evidenced by the lack of magnetite formation in serpentinized dunite, in which silica is not supplied by any reactions. Coleman and Keith (1971) have made a similar observation that serpentinized harzburgites contain more magnetite than serpentinized dunites in Burro Mountain peridotite, California. Bach et al. (2006), Beard et al. (2009), and Frost et al. (2013) argued that magnetite was formed along with serpentine by the breakdown of Fe-rich brucite with addition of aqueous silica in the second stage, which is essentially the same as reaction 2 of our model. Petrological observations and thermodynamic modeling by Frost et al. (2013) also demonstrated that the transition from brucite-serpentine to brucite-serpentine-magnetite assemblage is accompanied by an increase of oxygen fugacity with

a minor increase in silica activity. In fact, their thermodynamic model showed that increase only in silica activity could produce magnetite-serpentine assemblage (Figure 9 of Frost et al. 2013). Thus, it is likely that the magnetite formation promoted by addition of silica is a common reaction in many serpentinization systems. Consumption of silica by the magnetite formation reaction (reaction 2) and absence of talc in bastite (reaction 3) indicate that silica diffused from the locus of bastite formation to olivine-rich portions due to the gradient of silica activity. As suggested by Evans et al. (2013), this is the reason why hydration of orthopyroxene is not accompanied by talc, which can be produced by simple addition of water to orthopyroxene (e.g., Martin and Fife, 1970).

Katayama et al. (2010) suggested that magnetite is formed by the breakdown of Fe-rich serpentine via a silica-out reaction, on the basis of serpentine textures of a sample from Mineoka ophiolite, Japan, in which magnetite was found to occur in Si-poor zone at the center of magnetite-free serpentine veins. Serpentine-brucite veins were also observed outside the magnetite-free serpentine veins (Figure 2 of Katayama et al. 2010). These textures can be reinterpreted within the context of our two-stage model: the magnetite-free serpentine vein, magnetite-bearing Si-poor zone, and outer serpentine-brucite zone correspond to the type-B rim, brucite-magnetite vein, and type-A rim in our present study, respectively (Figure 7). The brucite-magnetite veins in our samples formed together with bastite at the second-stage reactions. Therefore, magnetite in the sample of Katayama et al. (2010) can also be considered to have formed by the addition of silica.

It should be noted that the mineralogical textures observed in this study (Figures 1, 7) are different in some aspects from those reported in previous studies (Bach et al. 2006; Beard et al. 2009; Frost et al. 2013). For example, two types of mesh rim reported by Beard et al. (2009) both contain brucite, whereas type-B rims of the Iwanaidake don't contain brucite (Figures 2, 3b).

412 Type-A and type-B rims of the Iwanaidake don't show any zoning (Figure 1a, b), but Klein et al.
413 (2009) and Frost et al. (2013) reported a zoned structure in mesh rims: brucite abundant on the
414 margins (in contact with olivine) and serpentine more abundant in the cores of the rims.
415 Serpentine in the mesh centers of the Iwanaidake samples seem to be in direct contact with relict
416 olivine (Figures 1d, 7), suggesting that the serpentine formed directly from hydration of olivine
417 (reaction 4), but such direct formation of serpentine from olivine has been rarely observed. These
418 differences in textures would have been caused by differences in many factors, such as bulk rock
419 composition, temperature, fluid/rock ratio, flow rate of fluid, and so on. Further work is required
420 to clarify the cause of this issue.
421
422 **Implications**
423 The changes in mineralogical textures with the progress of serpentinization in the Iwanaidake
424 ultramafic body demonstrate that serpentinization reactions proceeded via a two-stage process,
425 and that magnetite formation was associated with serpentinization of orthopyroxene in the second
426 stage (Figure 6). This suggests that the supply of silica component from serpentinization of
427 orthopyroxene is a trigger for the magnetite formation during serpentinization, as also evidenced
428 by the lack of magnetite formation in serpentinized dunite, in which there is no orthopyroxene.
429 Magnetite has extremely high magnetic susceptibility and electrical conductivity among mantle
430 minerals, and electro-magnetic anomalies of the seafloor have often been considered to indicate
431 the extent of serpentinization in the oceanic crust and underlying mantle (e.g., Nazarova 1994).
432 The magnetite formation during serpentinization also results in the production of hydrogen (e.g.,
433 reactions 2 and 4), which may activate microbial communities on the seafloor. Our observations
434 have shown that serpentinization of ultramafic rocks is not necessarily associated with magnetite
435 formation when silica component is not supplied. Therefore, supply of silica from outside or the

presence of silica-rich phases, such as orthopyroxene, in ultramafic lithologies that are being serpentinized would be one of the key factors to control the electro-magnetic properties of serpentinized mantle domains, as we as the activity of serpentinite-hosted microbial systems on the modern and ancient seafloors. Thus, thorough petrologic investigations of serpentinized ultramafic bodies would benefit to deepen our understanding of the role of serpentinization for the geodynamics of the Earth's interior and biological activities on the Earth's surface.

Acknowledgments

We thank K. Yoshida, S. Ohi, F. Higashino, T. Hirajima, T. Kawakami for their support in electron microprobe analysis, laser Raman analysis and discussion. We also thank T. Katoh for his great help during the sampling around Iwanaidake as well as his helpful suggestions and discussion, T. Azuma for his support during sampling, K. Hirauchi for his helpful comments on an earlier version of the manuscript, K. Matsukage and K. Kubo for useful information on Iwanaidake area, and S. Omori for useful discussion. Sampling around Iwanaidake was performed with the permission of Hatanaka Shouwa Corporation. We thank the staff members of Hidaka-Mitsuiwa Quarry of Hatanaka Shouwa for their assistance during sampling. This paper benefited greatly from critical and constructive comments by Bernard W. Evans, B. Ronald Frost, and Joshua Feinberg. This work was supported by MEXT KAKENHI for Scientific Research on Innovative Areas (Grant no. 21109004) and the Earthquake Research Institute cooperative research program (2011-G-12) to TK.

References cited

Allen, D.E., and Seyfried Jr., E. (2003) Compositional controls on vent fluids from ultramafic-hosted hydrothermal systems at mid-ocean ridges: an experimental study at 400°C, 500

bars. Geochimica et Cosmochimica Acta, 67, 1531-1542.

Bach, W., Paulick, H., Garrido, C.J., Ildefonse, B., Meurer, W.P., and Humphris, S.E. (2006) Unraveling the sequence of serpentinization reactions: petrography, mineral chemistry and petrophysics of serpentinites from MAR 15°N (ODP Leg 209, Site 1274). Geophysical Research Letters, 33, L13306, doi:10.1029/2006GL025681.

Beard, J., Frost, B.R., Fryer, P., McCaig, A., Searle, R., Ildefonse, B., Zinin, P., and Sharma, S. K. (2009) Onset and Progression of serpentinization and magnetite formation in olivine-rich troctolite from IODP Hole U1309D. Journal of Petrology, 50, 387–403.

Coleman, R.G., and Keith, T.E. (1971) Achemical study of serpentinization–Burro Mountain, Calfornia. Journal of Petrology, 12, 311-328.

Dearing, J. (1999) Environmental Magnetic susceptibility: Using the Bartington MS2 System, 2nd ed., 54 p. Chi Publishing, Kenilworth.

Dyment, J., Arkani-Hamed, J., and Ghods, A. (1997) Contribution of serpentinized ultramafics to marine magnetic anomalies at slow and intermediate spreading centres: insights from the shape of the anomalies. Geophysical Journal International, 29, 691–701.

Escartin, J., Hirth, G., and Evans, B. (1997) Effects of serpentinization on the lithospheric strengthen and the style of normal faulting at slow-spreading ridges. Earth and Planetary Science Letters, 151, 181–189.

Evans, B.W. (2008) Control of the products of serpentinization by the $Fe^{2+}Mg_{-1}$ exchange potential of olivine and orthopyroxene. Journal of Petrology, 49, 1873–1887.

Evans, B.W. (2010) Lizardite versus antigolite serpentinite: Magnetite, hydrogen, and life(?). Geology, 38, 879–882.

Evans, B.W., Hattori, K., and Baronnet, A. (2013) Serpentinite: what, why, where? Elements, 9, 99-106.

Frost, B.R., and Beard, J.S. (2007) On silica activity and serpentinization. Journal of Petrology, 48, 1351–1368.

Frost, B.R., Evans, K.A., Swapp, S.M., Beard, J.S., and Mothersole, F.E. (2013) The process of serpentinization in dunite from New Caledonia. Lithos, 178, 24-39.

Hirauchi, K., Katayama, I., Uehara, S., Miyahara, M., and Takai, Y. (2010) Inhibition of subduction thrust earthquakes by low-temperature plastic flow in serpentine. Earth and Planetary Science Letters, 295, 349–357.

Ishizuka, H., Imaizumi, M., Gouchi, N., and Banno, S. (1983) The Kamuikotan zone in Hokkaido, Japan: Tectonic mixing of high-pressure and low-pressure metamorphic rocks. Journal of Metamorphic Geology 1, 263–275.

Katayama, I., Hirauchi, K., Michibayashi, K., and Ando, J. (2009) Trench-parallel anisotropy produced by serpentine deformation on the hydrated mantle wedge. Nature, 461, 1114–1117.

Katayama, I., Kurosaki, I., and Hirauchi, K. (2010) Low silica activity for hydrogen generation during serpentinization: An example of natural serpentinites in the Mineoka ophiolite complex, central Japan. Earth and Planetary Science Letters, 298, 199–204.

Katoh, T. (1978) The Saru-gawa ultramafic massif in Kamuikotan belt, central axial zone of Hokkaido. Earth Science (Chikyu Kagaku), 32, 273–279 (in Japanese with English abstract).

Katoh, T., and Nakagawa, M. (1986) Tectogenesis of ultramafic rocks in the Kamuikotan tectonic belt, Hokkaido, Japan. Association for the Geological Collaboration in Japan Monograph, 31, 119–135 (in Japanese with English abstract).

Kimura, G. (1986) Oblique subduction and collision: Forearc tectonics of the Kuril arc. Geology, 14, 404–407.

508 Klein, F., Bach, W., Jöns, N., McCollom, T., Moskowitz, B., and Berquó, T. (2009) Iron
509 partitioning and hydrogen generation during serpentinization of abyssal peridotites from
510 15°N on the Mid-Atlantic Ridge. Geochimica et Cosmochimica Acta, 73, 6868–6893.
511 Kubo, K. (2002) Dunite formation processes in highly depleted peridotite: Case study of the
512 Iwanaidake peridotite, Hokkaido, Japan. Journal of Petrology, 43, 423–446.
513 Maher, B.A. (1988) Magnetic properties of some synthetic sub-micron magnetites. Geophysical
514 Journal International, 94, 83–96.
515 Martin, B., and Fyfe, W.S. (1970) Some experimental and theoretical observations on the kinetics
516 of hydration reactions with particular reference to serpentinization. Chemical Geology, 6,
517 185-202.
518 Martin, W., Baross, J., Kelley, D.S., and Russell, M.J. (2008) Hydrothermal vents and the origin
519 of life. Nature Reviews Microbiology, 6, 805–814.
520 Mèvel, C. (2003) Serpentinization of abyssal peridotite at mid-ocean ridges. Comptes Rendus
521 Geoscience, 335, 825–852.
522 Nazarova, K.A. (1994) Serpentinized peridotites as a possible source for oceanic magnetic
523 anomalies. Marine Geophysical Researches, 16, 455-462.
524 Nealson, K.H., Inagaki, F., and Takai, K. (2005) Hydrogen-driven subsurface lithoautotrophic
525 microbial ecosystems (SLiME): Do they exist and why should we care? Trends in
526 Microbiology, 13, 405–410.
527 Noguchi, Y., Toramaru, A., and Shimano, T. (2006) Crystallization of microlites and degassing
528 during magma ascent: constraints on the fluid mechanical behavior of magma during the
529 Tenjo Eruption on Kozu Island, Japan. Bulletin of Volcanology, 68, 432-449.
530 Oufi, O., Cannat, M., and Horen, H. (2002) Magnetic properties of variably serpentinized abyssal
531 peridotites. Journal of Geophysical Research 107, doi: 10.1029/2001JB000549.

532 Plümper, O., King, H.E., Vollmer, C., Ramasse, Q., Jung, H., and Austrheim, H. (2012) The
533 legacy of crystal-plastic deformation in olivine: high-diffusivity pathways during
534 serpentinization. Contributions to Mineralogy and Petrology, 163, 701–724.
535 Rinaudo, C., Gastaldi, D., and Belluso, E. (2003) Characterization of chrysotile, antigorite and
536 lizardite by FT-Raman spectroscopy. Canadian Mineralogist, 41, 883–890.
537 Seyfried, W.E. Jr., Foustoukos, D.I., and Fu, Q. (2007) Redox evolution and mass transfer during
538 serpentinization: An experimental and theoretical study at 200°C, 500 bar with
539 implications for ultramafic-hosted hydrothermal systems at Mid-Ocean Ridges.
540 Geochimica et Cosmochimica Acta, 71, 3872–3886.
541 Sleep, N.H., Meibom, A., Fridriksson, T., Coleman, R.G., and Bird, D.K. (2004) H_2-rich fluids
542 from serpentinization: Geochemical and biotic implications. Proceedings of the National
543 Academy of Sciences of the United States of America, 104, 12818–12823.
544 Takai, K., Gamo, T., Nakagawa, N., Hirayama, N., Nealson, K.H., and Horikoshi, K. (2004)
545 Geochemical and microbiological evidence for an hydrogen-based, hyperthermophilic
546 subsurface lithoautotrophic microbial ecosystem (Hyper-SLiME) beneath an active deep-
547 sea hydrothermal field. Extremophiles, 8, 269–282.
548 Toft, P.B., Arkani-Hamed, J., and Haggerty, S.E. (1990) The effect of serpentinization on density
549 and magnetic susceptibility: a petrophysical model, Physics of the Earth and Planetary
550 Interiors 65:137–157.
551

552 **Figure captions:**

553

554 **Figure 1.** Photomicrographs of serpentinized harzburgite. Abbreviations: Ol = olivine, Brc =
555 Brucite, Mgt = magnetite. **(a)** Serpentine mesh texture with type-A and type-B rims (plane-
556 polarized light). **(b)** Enlarged photo of the center of **a** (cross-polarized light with sensitive color
557 plate). The type-A rim (orange) is in contact with relic olivine, and is surrounded by the type-B
558 rim (blue). Brucite-magnetite veins occur between two adjacent areas of type-B rim. **(c)** Mesh
559 texture with type-B rims (plane-polarized light). Brucite-magnetite veins are also sandwiched by
560 type-B rims here. **(d)** Mesh-center serpentine surrounded by both type-A and type-B rims (plane
561 polarized light).

562

563 **Figure 2.** FeO-MgO-SiO_2 ternary diagram (molar proportions) of mineralogical textures.
564 Compositions of type-A rims plot along a line that connects serpentine (Mg#94) with brucite
565 (Mg#86). Data of brucite-magnetite veins represent the compositions of the mixtures of brucite in
566 the veins and adjacent type-B serpentine. They plot along a line that connects the Mg-rich end of
567 Type-B serpentine (Mg#96) and brucite (Mg#89), indicating that the brucite-magnetite veins
568 contain Mg#89 brucite. Compositions of mesh-center serpentine in serpentinized dunite are
569 similar to those of type-A rims.

570

571 **Figure 3.** Plots of Si + Al/2 + Cr/2 cations versus Fe cations per seven oxygen formula unit. **(a)**
572 Compositions of type-A rims and relic olivine in harzburgite and dunite. All data lie along a trend
573 connecting brucite (Mg#86) and serpentine (Mg#94). The trend doesn't deviate to the direction of
574 Mg-cronstedtite or silica. **(b)** Compositions of type-B rims and brucite in brucite-magnetite veins
575 in harzburgite. Data of brucite (filled triangles) plot along a trend connecting brucite (Mg#89)

and serpentine (Mg#96). Data of type-B rims (filled circles) plot along a trend connecting serpentine (Mg#96) and Fe^{3+}-serpentine-bearing serpentine with Mg#92 (gray circle). **(c)** Compositions of serpentine in mesh centers of harzburgite and dunite. Data of harzburgite plot along a trend toward Fe^{3+}-serpentine. Data of dunite plot along a trend connecting brucite (Mg#86) and serpentine (Mg#94), which is the same as that in **a**. **(d)** Compositions of bastites and relic orthopyroxene in harzburgite. Data of bastites plot along a trend toward Fe^{3+}-serpentine.

Figure 4. Modal changes of mineralogical textures. The vertical axis corresponds to modal composition. Samples are aligned in the order of degree of serpentinization. **(a)** Mode changes in serpentinized harzburgite. Type-A rims are abundant in weakly serpentinized samples (0 to ~40 vol% of serpentinization), whereas type-B rims become dominant in highly serpentinized samples. Type-B rims appear concurrently with bastite and mesh-center serpentine. **(b)** Modal changes in serpentinized dunite. The modes of type-A rims and mesh-center serpentine increase with increasing degree of serpentinization.

Figure 5. Degree of serpentinization vs. magnetic susceptibility. Arrows were calculated following the procedures of Toft et al. (1990). The solid arrow is for the first-stage serpentinization (reaction 1), and the dashed arrow is for the second stage serpentinization (reactions 2-4). See text for details. It is assumed that the second-stage reactions start when the degree of serpentinization reaches 30 vol%. The densities of the component minerals have been assumed as follows (unit in g/cm^3): serpentine 2.6, brucite 2.5, magnetite 5.2, olivine 3.2, and orthopyroxene 3.2.

Figure 6. Degree of serpentinization vs. bulk H_2O content. The solid arrow represents the result

of calculation for the first-stage serpentinization (reaction 1), and the dashed arrow for the second-stage serpentinization (reactions 2–4). Symbols are as in Figure 4.

Figure 7. Summarized illustrations of the progress of serpentinization reactions in Iwanaidake ultramafic rocks. Abbreviations: Ol = olivine, Opx = orthopyroxene. **(a)** Two-stage serpentinization of harzburgite. Type-A rims (orange) are formed during the first stage. Type-B rims (white) and brucite-magnetite veins (blue with black dots) replace the type-A rims during the second stage when bastite (gray) is formed. Serpentinization of mesh center (green) also occurs during the second stage. **(b)** Single-stage serpentinization of dunite. Type-A rims are formed earlier, and then mesh-center serpentines are formed.

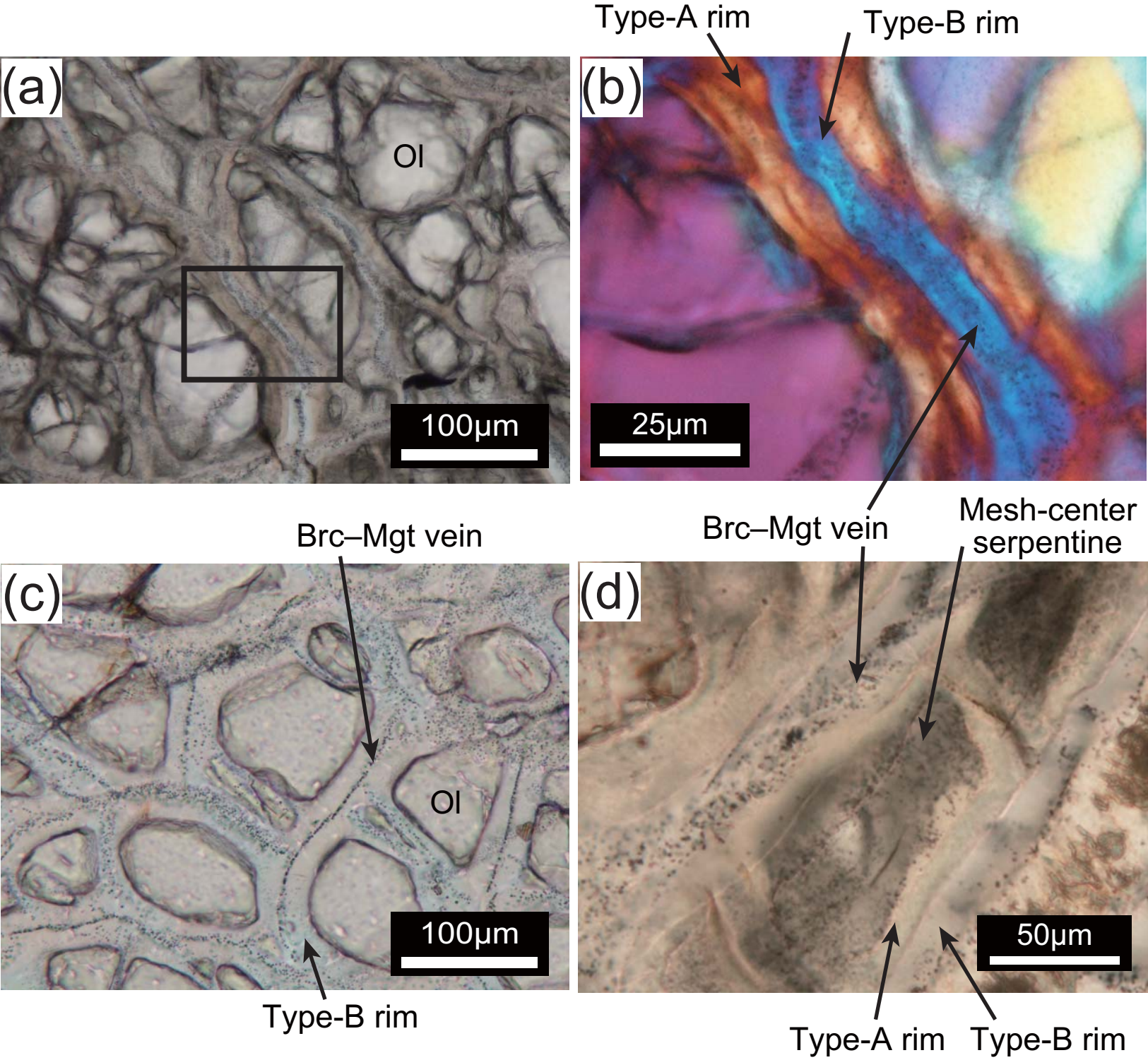

Figure 1 Miyoshi et al.

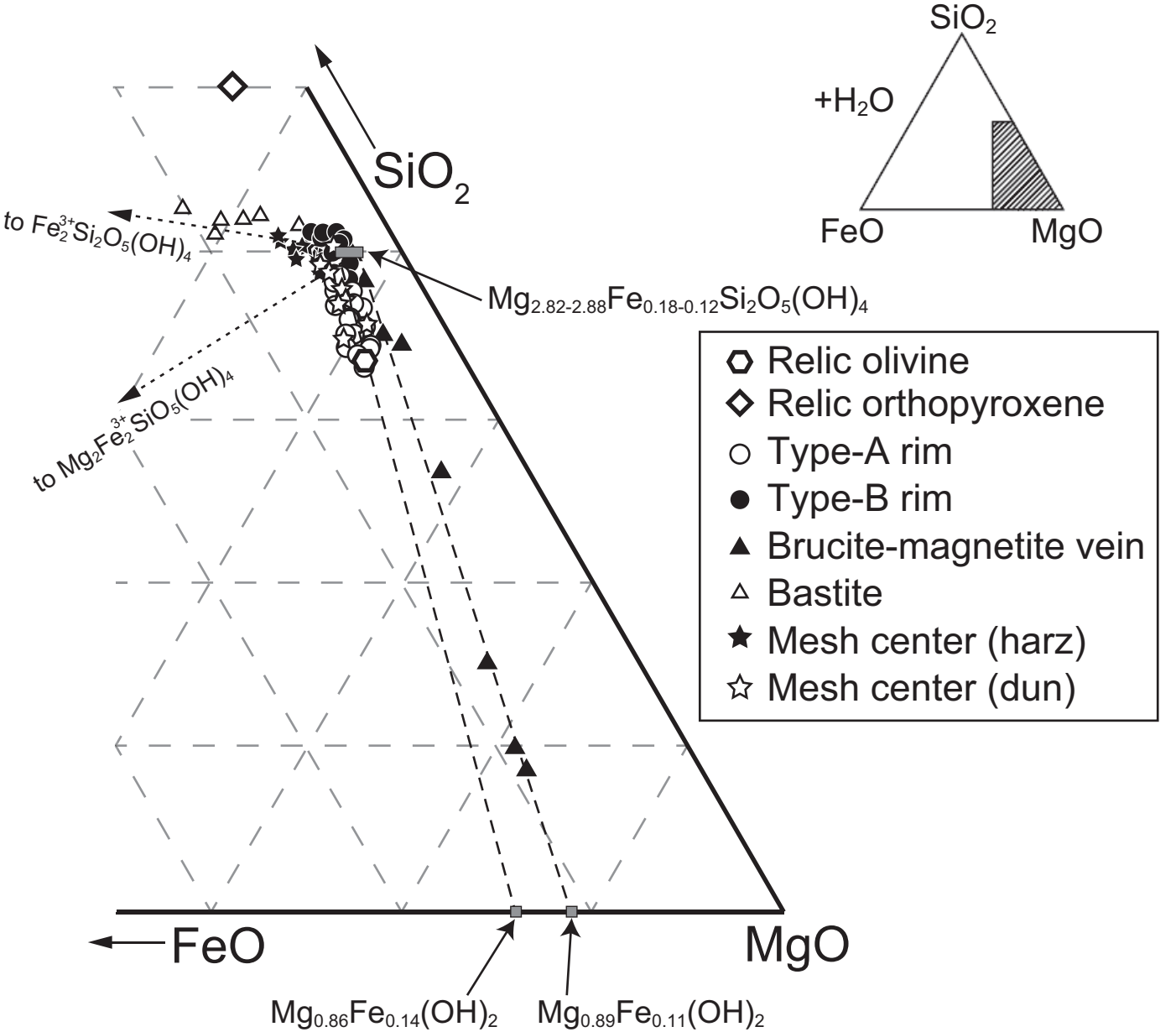

Figure 2 Miyoshi et al.

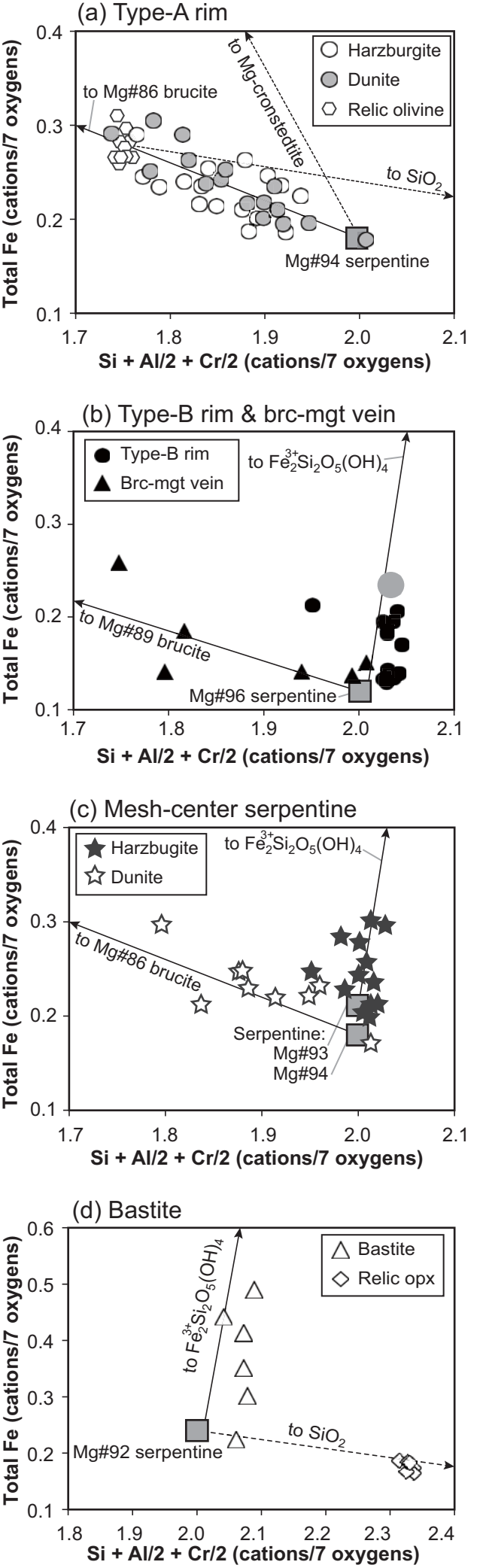

Figure 3 Miyoshi et al.

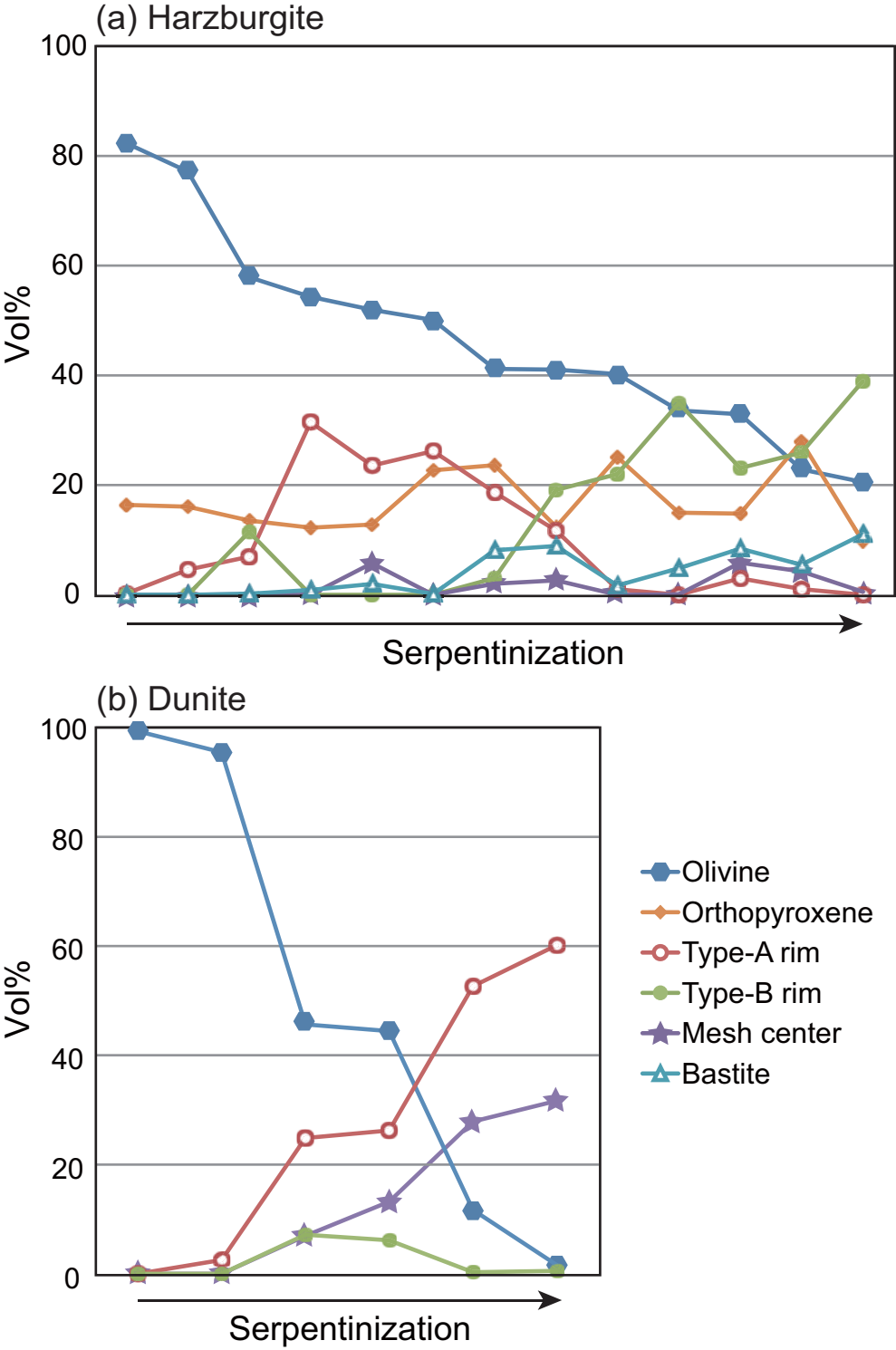

Figure 4 Miyoshi et al.

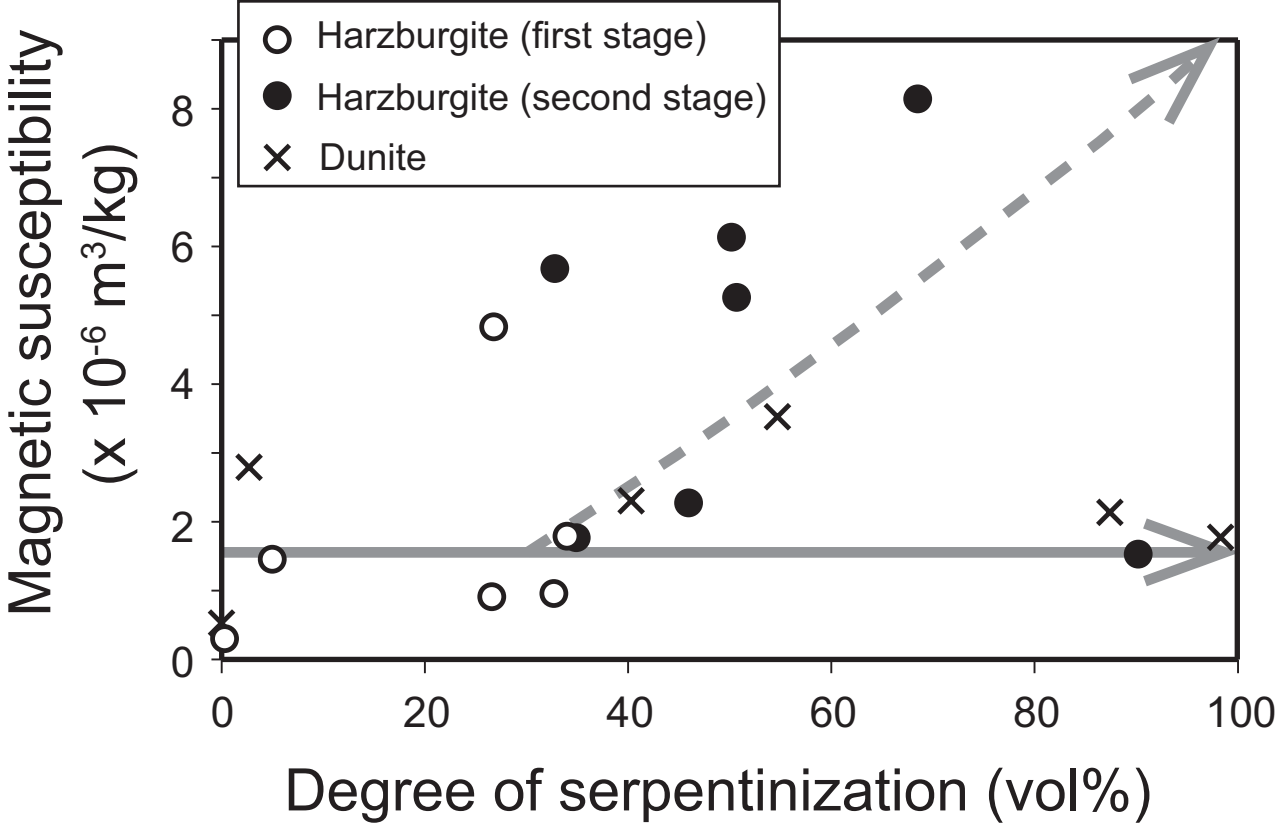

Figure 5 Miyoshi et al.

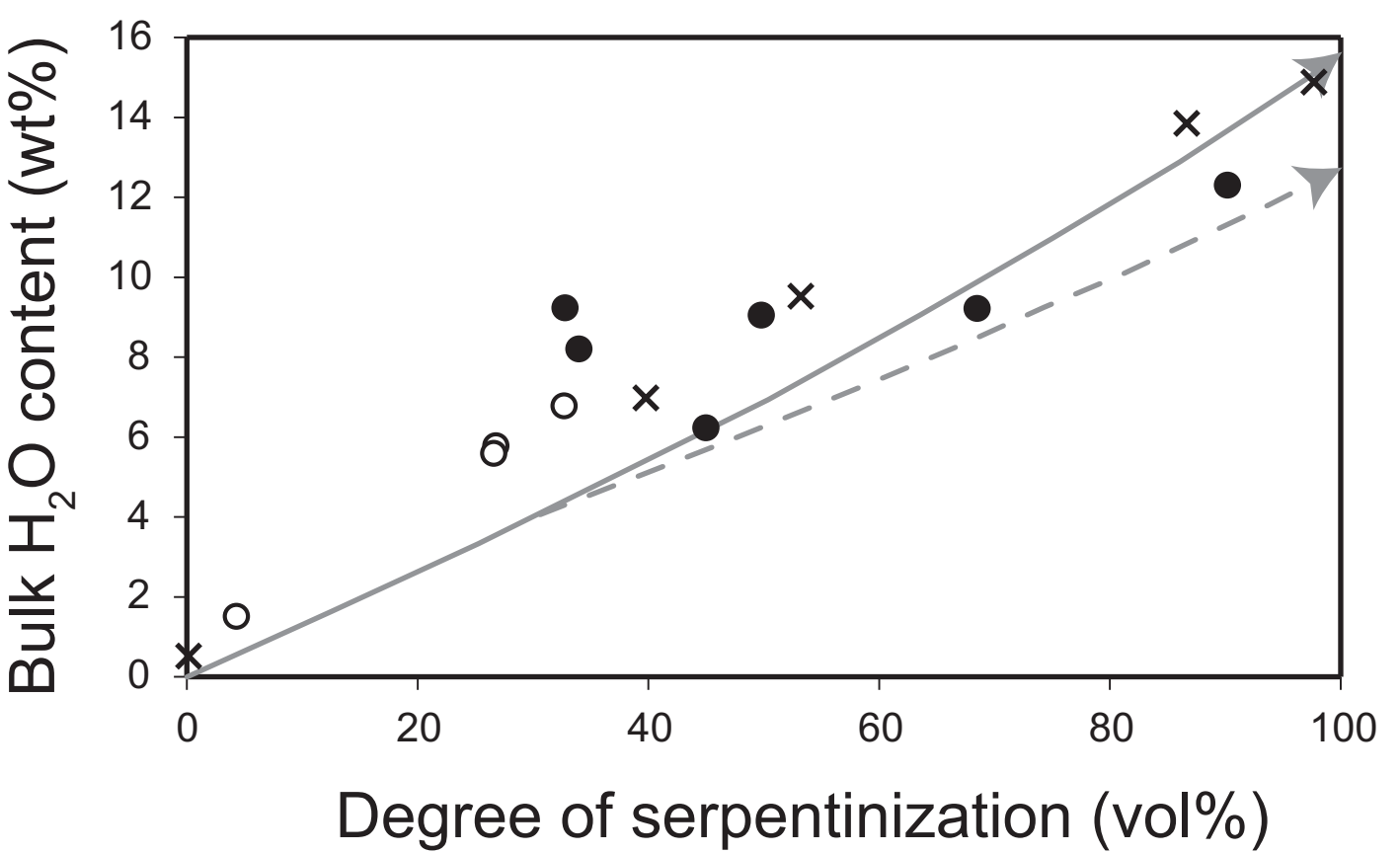

Figure 6 Miyoshi et al.

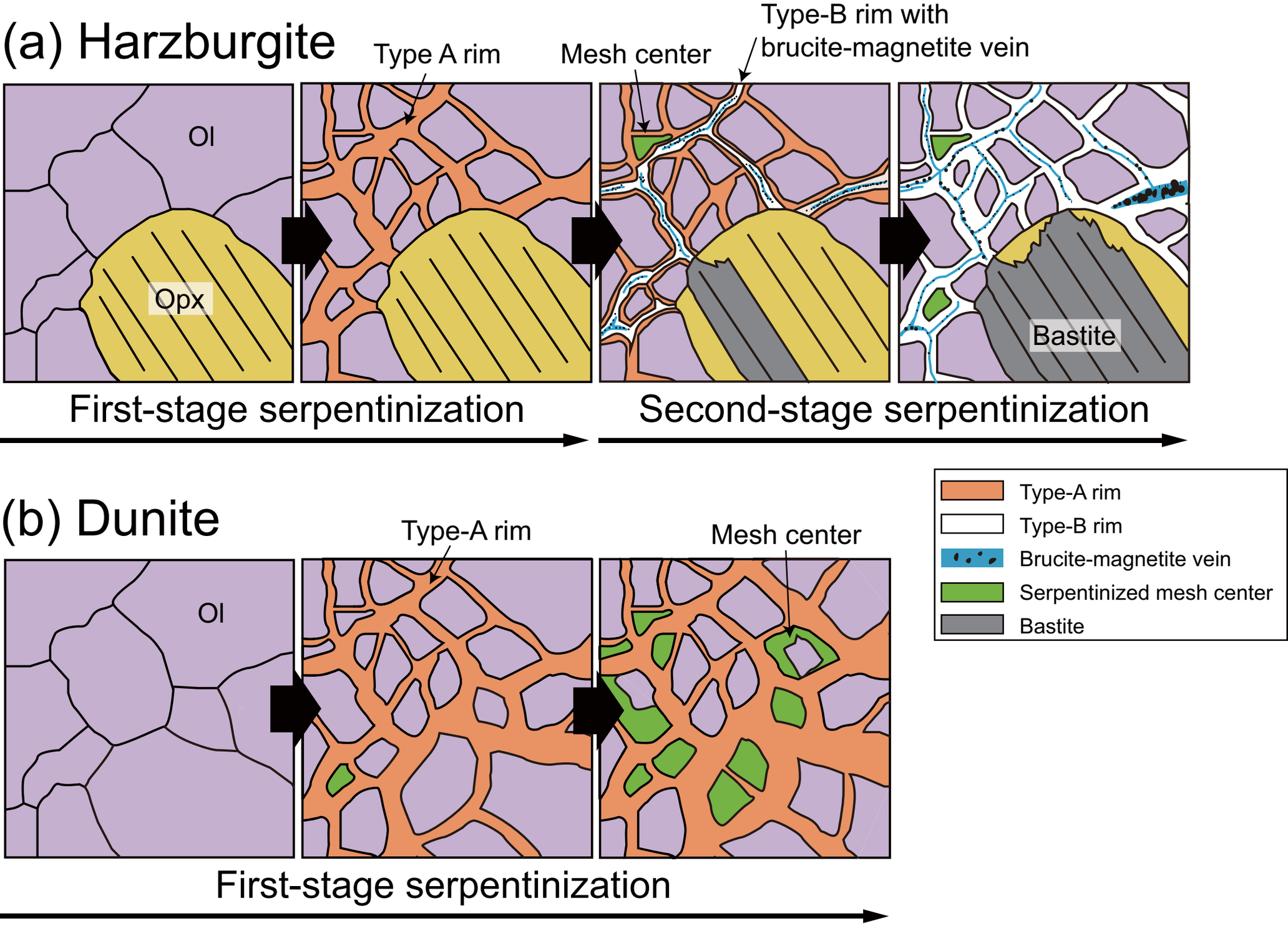

Figure 7 Miyoshi et al.

Table 1. Modal composition, magnetic susceptibility, and bulk H_2O content of serpentinized harzburgite and dunite samples from Iwanaidake ultramafic body.

Rock type of protolith	Harzburgite														Dunite						
Sample name	Iw02n	Iw05c	Iw07a	Iw08b	Iw10b	Iw10e	Iw11g	Iw12a	Iw13a	Iw14a	Iw15e	Iw16a	Iw18a	Iw18b	Iw02c	Iw06c	Iw07d	Iw08a	Iw08d	Iw15a	Iw15c
Modal composition (vol%)																					
Olivine	41.2	40.3	54.3	82.4	57.9	52.0	50.1	32.9	20.6	22.9	2.1	33.6	41.1	77.2	1.6	45.7	11.7	95.5	99.3	44.5	58.1
Orthopyroxene	23.7	25.1	12.3	16.4	13.6	12.8	22.7	14.8	9.7	28.0	7.4	15.0	12.4	16.1	0.0	0.0	0.0	0.3	0.0	0.3	0.4
Spinel	0.5	0.8	0.6	1.1	0.9	0.9	0.6	1.2	0.3	0.6	0.0	0.9	0.7	1.6	0.9	0.4	1.2	0.7	0.7	0.4	1.0
Serpentine texture																					
Type-A rim	18.7	1.0	31.5	0.3	7.0	23.6	26.2	3.0	0.0	1.1	-	0.0	11.7	0.0	60.2	24.9	52.7	2.5	0.0	26.3	21.7
Type-B rim	3.1	22.0	0.0	0.0	11.4	0.0	0.0	23.1	39.0	25.9	-	35.0	19.1	0.0	0.6	7.2	0.3	0.0	0.0	6.2	5.0
Mesh center	2.1	0.0	0.0	0.0	0.1	5.8	0.0	5.9	0.6	4.3	-	0.1	2.7	0.0	31.7	7.0	27.9	0.0	0.0	13.2	5.6
Bastite	8.1	1.7	0.9	0.0	0.2	2.0	0.2	8.4	11.0	5.5	-	4.9	8.9	0.0	0.0	0.0	0.0	0.2	0.0	0.1	0.0
Later-stage vein	0.8		0.3	0.0	0.0	1.2	0.2	0.3	0.2	2.2	-	0.0	0.2	4.6	4.4	0.0	6.1	0.0	0.0	0.0	0.0
Not classified [a]	-	-	-	-	-	-	-	-	-	-	86.1	-	-	-	-	-	-	-	-	-	-
Brucite	1.5	7.2	0.0	0.0	7.5	0.8	0.0	8.7	15.2	6.5	1.1	9.1	2.2	0.0	0.0	13.1	0.0	0.0	0.0	8.1	7.2
Magnetite	0.6	2.1	0.3	0.0	1.5	1.2	0.1	1.8	3.6	3.3	3.4	1.7	1.3	0.6	0.8	2.0	0.2	1.0	0.0	1.1	1.2
Degree of serpentinization [b]	33.8	32.5	32.6	0.3	26.6	32.8	26.4	50.1	68.3	45.7	90.2	49.8	45.1	0.0	97.4	53.1	86.2	2.6	0.0	54.4	39.9
Magnetic susceptibility [c] ($\times 10^{-6}$	1.79	5.68	0.96	0.30	4.83	1.79	0.91	5.26	8.14	2.27	1.53	6.13	-	1.46	1.77	-	2.14	2.80	0.53	3.57	2.31
H_2O content [c] (wt%)	8.2	9.1	6.8	-	5.6	-	5.6	-	9.3	-	12.3	9.0	6.2	1.62	14.9	9.6	13.9	-	0.5	-	7.0

Notes: [a] Serpentine that cannot be classified into any texture types because of complete destruction of mesh texture by intense serpentinization. [b] The modes of later-stage vein and magnetite are not included in calculating degree of serpentinization. [c] Standard deviations (1 sigma) are on the order of 10^{-10} m^3/kg for the magnetic susceptibility measurement and < 0.1 wt% for the Karl-Fischer measurement of H_2O content (Noguchi et al. 2006).